Application of the embedded atom method to Ni_3Al

S. M. Foiles and M. S. Daw
Sandia National Laboratories, Livermore, California 94550

(Received 28 August 1986; accepted 17 November 1986)

The embedded atom method [M. S. Daw and M. I. Baskes, Phys. Rev. **B 29**, 6443 (1984)] is used to calculate phase stability, lattice vibrational frequencies, point defect properties, antiphase boundary energies, and surface energies and relaxations for Ni_3Al. The empirical embedding functions and core–core repulsions used by this method are obtained. The equilibrium phases for the Ni-rich half of the composition range of Ni–Al are determined for 1000 K and compared with experiment. The elastic constants and vibrational modes of Ni_3Al are calculated and the elastic constants are compared with experiment. The formation energy, formation volume, and migration energies of vacancies are computed, and it is found that the formation energy of vacancies on the Ni sublattice is less than that on the Al sublattice. The (100) antiphase boundary is shown to be significantly lower in energy than the (111) antiphase boundary. The surface energies and atomic relaxations of the low index faces are computed, and it is shown that for the (100) and (110) faces that the preferred surface geometry corresponds to the bulk lattice with the mixed composition plane exposed.

I. INTRODUCTION

There is a great deal of current interest in the Ni_3Al alloy due to its unusual mechanical properties. Nickel aluminide forms an $L1_2$ ordered crystal structure.[1] The long-range ordering is responsible for its unusual mechanical property of increasing yield stress with increasing temperature.[2] The Ni_3Al-based alloys are also resistant to air oxidation due to their ability to maintain an adherent surface oxide film.[3] An inherent drawback to using monolithic Ni_3Al as a structural material is the tendency of a polycrystalline pure stoichiometric alloy to undergo brittle intergranular fracture. However, recent work has shown that nonideal stoichiometry combined with certain alloy additions, in particular, boron, produces a ductile polycrystalline material.[4] Finally, Ni_3Al is the most important strengthening constituent of commercial nickel-based alloys and is responsible for these alloys' high-temperature strength and creep resistance.

In this paper the first results of the application of the embedded atom method[5] (EAM) to the description of Ni–Al alloys are presented. The EAM is a recently developed technique for rapidly computing the total energy of an arbitrary arrangement of atoms in a metal or alloy. The energy is determined from the energy to embed each atom in the electron density due to the surrounding atoms plus a short-range core–core repulsion. The embedding functions and core–core repulsions are determined empirically by fitting to properties of the bulk material. The EAM has been applied successfully to a wide range of problems in pure metals including surfaces,[5,6] defect energies,[5,7] fracture,[5,8] phonons,[9] and liquid metals.[10] For binary alloys it has been used to determine the segregation at surfaces and internal defects in binary alloys containing Cu, Ag, Au, Ni, Pd, and Pt.[7,11] The technique has also been used successfully to study the interaction of hydrogen with metal surfaces.[5,12]

In this work the EAM will be used to compute the energies of point defects, antiphase boundaries, and surfaces of Ni_3Al as well as the vibrational properties of the alloy. Section II summarizes the EAM and presents the empirically determined embedding functions and core–core repulsions used to describe the Ni–Al system. In Sec. III the predictions of the method for the equilibrium phases of Ni–Al alloys for Al concentrations of less than 50% will be compared with the known phase diagram to provide a test of the validity of the functions. Another test of the functions is provided in Sec. IV, where the elastic constants and vibrational modes of Ni_3Al are computed and the elastic constants are compared to experiment. Section V presents the computations of point defect properties including the vacancy formation and migration energies in Ni_3Al as well as the divacancy binding energy. Next, results of computations of the (100) and (111) antiphase boundary energies will be discussed. The final section describes the results obtained for the energy, relaxation, and preferred composition of the low index surfaces of Ni_3Al.

II. THEORY

In order to calculate the structure and energetics of defects and inhomogeneities in metal alloys, the total energy of the system must be known for an arbitrary arrangement of the atoms. In practice this prescription must be computationally simple to allow for the relaxation of the atomic coordinates, to perform a statistical analysis of thermal effects, or to study dynamics. Tradi-

 0003-6951/87/010005-11$01.75

tionally, these classes of problems have been addressed by assuming that the total energy of the solid is the sum of pair interactions between the atoms. While this approximation is useful in many cases, it has certain shortcomings. First, in order to properly describe the elastic constants, this approach requires an energy contribution that depends on the overall density or volume of the system.[13] It is not clear, though, how to treat this contribution to the energy at extended defects, for example, surfaces and grain boundaries. For alloys the pair interaction approach requires the determination of the pair interaction between unlike atoms as well as the variation of the volume-dependent contribution with alloy composition. The EAM is an attempt to provide a new method of determining the total energy that avoids some of these difficulties while retaining the computational simplicity of the pair interaction approach.

The total energy of an arbitrary arrangement of atoms can be written as a unique functional of the total electron density. The starting point of the embedded atom method is the observation that the total electron density in the vicinity of a given atom can be thought of as the atomic density of the atom in question plus a background electron density contributed by the surrounding atoms. This latter contribution to the total electron density is a slowly varying function of position, and so it is reasonable to approximate this contribution to the local electron density by a constant. The energy of this atom can then be approximated by the energy associated with the electron density of the atom plus this constant background density. This defines an embedding energy for that atomic species as a function of the background electron density. There is an additional electrostatic energy contribution due to core–core overlap. These ideas have been developed by Daw[14] and Daw and Baskes[5] who show that the total energy can be written approximately as

$$E_{\text{tot}} = \sum_i F_i(\rho_i) + \frac{1}{2}\sum_{ij,i\neq j} \varphi_{ij}(R_{ij}). \tag{1}$$

In this expression ρ_i is the electron density at atom i due to the remaining atoms of the system, $F_i(\rho_i)$ is the energy to embed atom i into the electron density ρ_i, and $\varphi_{ij}(R_{ij})$ is the core–core repulsion between atoms i and j separated by the distance R_{ij}. The electron density is approximated by the superposition of atomic densities

$$\rho_i = \sum_{j\neq i} \rho_j^a(R_{ij}), \tag{2}$$

where $\rho_j^a(R)$ is the atomic electron density due to atom j at the distance R. With this approximation for the electron density, the actual computations using this method do not require significantly more work than the use of traditional pair interaction models. Note that the embedding energy $F_i(\rho_i)$, does not depend on the source of the background density. Thus the same embedding function would be used to calculate the energy of an atom in an alloy that would be used in the pure material. This makes this method particularly appealing for studies of alloys. Further, note that all the quantities used in this approach are well defined even in the presence of severe nonuniformities such as surfaces.

To apply this method the embedding energies, core–core repulsions, and atomic densities must be known. The atomic densities will be taken from free atom calculations. The embedding energies and core–core repulsions can be calculated from the formal definitions of these quantities in the density functional framework as described by Daw.[14] These values, though, give only qualitatively correct predictions of the material properties, so, in order to make quantitative predictions, it is necessary to determine these functions empirically using the first principles calculations as a guide to the form of the functions. The specific functions are determined by fitting to experimental data as described below. The procedure used here is very similar to that used previously to study the alloys of Ni, Pd, Pt, Cu, Ag, and Au.[7] That work successfully determined a wide range of defect and surface energies.

A great deal of information about the embedding function can be obtained through the equation of state of the expanded or compressed pure metals since the electron density at each lattice site can vary substantially with a reasonable change in volume. Rose *et al.*[15] have shown that the sublimation energy of most metals as a function of lattice constant can be scaled to a simple universal function. Here we will force the equation of state of the pure metals to obey a slightly modified form of this equation of state,

$$E(a^*) = \begin{cases} -E_s(1+a^*)e^{-a^*}, & a^* > 0, \\ -E_s\left(1 + \dfrac{a^*}{(1+\lambda a^*)^2} + 2\lambda a^{*2}\right)e^{-a^*}, & a^* < 0. \end{cases} \tag{3}$$

The quantity a^* is a measure of the deviation from equilibrium

$$a^* = (a/a_0 - 1)/\lambda. \tag{4}$$

In these expressions a is a length scale of the system that we will take to be the face-centered cubic (fcc) lattice constant, a_0 is the equilibrium lattice constant, and E_s is the absolute value of the equilibrium sublimation ener-

gy. The quantity λ is defined by

$$\lambda = \sqrt{E_s/9B\Omega}\,, \tag{5}$$

where B is the bulk modulus of the material at equilibrium and Ω is the volume per atom at equilibrium. Note that the only input data needed are the equilibrium lattice constant, sublimation energy, and bulk modulus of the material, which are generally readily available.

Given the atomic electron densities ρ^a and the core–core repulsion $\varphi(R)$, the embedding energy can be uniquely defined by requiring the total energy of the pure metal given by Eq. (1) to agree with the energy as a function of lattice constant, $E\{a^*(a)\}$, given by Eq. (3). In particular, if $\rho_{\rm tot}(a)$ is the background electron density of the pure material evaluated for the lattice constant a and $\varphi_{\rm tot}(a)$ is the sum of the core–core repulsions, the second term in Eq. (1) also evaluated for the pure material with a lattice constant of a, then

$$F(\rho_{\rm tot}(a)) = E\{a^*(a)\} - \varphi_{\rm tot}(a). \tag{6}$$

The remaining task is to determine the atomic electron densities and pair interactions. The atomic electron densities are assumed to be given by the free atom densities calculated from Hartree–Fock theory by Clementi and Roetti.[16] There is one ambiguity, though, in using these electron densities for the bulk. While the optimum electronic configuration or orbital occupation is known for the free atom, it is not necessarily true that this configuration will be the best representation of the electron density in the solid. The atomic electron densities in this work are computed from the Hartree–Fock wave functions by

$$\rho^a(R) = N_s\rho_s(R) + N_p\rho_p(R) + N_d\rho_d(R), \tag{7}$$

where N_s, N_p, and N_d are the number of outer s, p, and d electrons and ρ_s, ρ_p, and ρ_d are the electron densities associated with the s, p, and d Hartree–Fock wave functions. (For Ni the wave functions for the $3d^8 4s^2$ configuration are used, while for Al the wave functions are for $3s^2p^1$.) The total number of outer electrons is fixed to the number of valence electrons of the neutral atom with the additional constraints $N_p = 0$ for Ni and $N_d = 0$ for Al. Thus the atomic density of each species depends on the single parameter, N_s. As will be discussed below, this parameter will be determined as part of the fitting procedure.

The last quantity that is needed is the core–core repulsion term. The form of this function has been studied from first principles by Daw.[14] This analysis shows that the core–core repulsion between atoms of different atomic species is accurately approximated by the geometric mean of the repulsion for the two pure metals. This and the electrostatic origin of this term suggests writing the core–core repulsion between atoms i and j as

$$\varphi_{ij}(R) = Z_i(R)Z_j(R)/R, \tag{8}$$

TABLE I. Parameters used to define the effective charge for the core–core repulsion (Eq. 7) and the atomic densities (Eq. 5). The effective charge is in units of electron charge and the values are for distances in Å.

	Z_0	α	β	ν	N_s	R_c
Ni	17.417	1.454	0.352	2.0	2.0	4.8
Al	16.711	1.058	0.110	1.0	1.640	5.5

where the effective charge $Z(R)$ for each element is computed from the functional form

$$Z(R) = Z_0(1 + \beta r^\nu)e^{-\alpha R} \tag{9}$$

and Z_0, α, β, and ν are fitting parameters. Finally, for the sake of computational efficiency, the atomic densities and core–core repulsions are cut off at a distance R_c. [Both the effective charge, $Z(R)$, and the atomic electron density are set to zero beyond R_c, and inside R_c a constant is added so that the functions go to zero continuously at the cutoff distance.]

The various parameters required to define the core–core repulsion and atomic densities have been determined empirically by fitting to the elastic constants and vacancy formation energy of the pure metals nickel and aluminum and to the sublimation energies and lattice constants of the ordered alloys NiAl, with the CsCl structure, and Ni_3Al, with the Cu_3Au structure. Note that due to the definition of the embedding function in terms of the equation of state of the pure metals, the

TABLE II. Experimental pure metal properties used to determine the functions: equilibrium lattice constants, sublimation energy, bulk modulus, elastic constants, and vacancy formation energy. Where two numbers are given, the top number is the value resulting from the fitting procedure and the lower number is the experimental value.

	Ni	Al
a_0 (Å)	3.52	4.05
$E_{\rm sub}$ (eV)[a]	4.45	3.58
B (10^{12} ergs/cm^3)[b]	1.804	0.81
C_{11} (10^{12} ergs/cm^3)[b]	2.587	1.08
	2.465	1.12
C_{12} (10^{12} ergs/cm^3)[b]	1.412	0.68
	1.473	0.66
C_{44} (10^{12} ergs/cm^3)[b]	1.299	0.45
	1.247	0.28
E_v^f (eV)	1.51	0.64
	1.6[c]	0.7[d]

[a] Reference 17.
[b] Reference 18.
[c] Reference 19.
[d] Reference 20.

TABLE III. Comparison of the experimental lattice constants a and excess enthalpies ΔH for the ordered alloys NiAl (CsCl structure) and Ni_3Al (Cu_3Au structure) with the values resulting from the fitting procedure.

	a_{fit} (Å)	a_{exp} (Å)[a]	ΔH_{fit} (eV)	ΔH_{exp} (eV)[b]
Ni_3Al	3.566	3.570	−0.40	−0.39
NiAl	2.891	2.887	−0.49	−0.61

[a] Reference 1.
[b] Reference 22.

equilibrium lattice constant, sublimation energy, and bulk modulus are guaranteed to be correct for the pure metals. The parameters used to define the core–core repulsion and atomic densities are given in Table I. Table II compares the calculated pure metal properties to the experimental values used in the fitting procedure. Table III shows the experimental lattice constant and excess enthalpies for the alloys, again compared with the calculated values resulting from the fitting procedure. In general the agreement between the fitted and experimental values is quite good. The poorest agreement is for the sublimation energy of the NiAl alloy and for the shear modulus C_{44} of Al. Note, however, that this work is primarily concerned with Ni_3Al and, as will be shown below, the elastic constants of that alloy are reproduced quite well.

The results of two types of calculations will be represented in this work. The first is energy minimization. These calculations predict the zero temperature enthalpy of the solid. Periodic boundary conditions are applied to avoid free surfaces. In the calculations presented below, the total energy of the system is minimized with respect to the independent motion of all the atoms in the computational cell and with respect to changes in the overall lattice constant. The second type of calculations presented here are Monte Carlo simulations. They are used to produce the thermal equilibrium atomic distribution of the atoms. These simulations allow for the atomic motion around the lattice sites. In addition, the calculations are performed in an isobaric, grand canonical ensemble where the relative value of the chemical potentials of the two species is held constant. The simulations allow the atomic species of an atom to change in accord with the change in the total energy relative to the chemical potential as described previously.[11] This procedure produces rapid convergence of the equilibrium compositional distribution since the need for actual atomic diffusion is bypassed. The desired pressure P is maintained by allowing the volume of the computational cell to change by a uniform dilation ΔV of the system.[22] The volume change is accepted based on the change in energy relative to $P\Delta V$.

III. EQUILIBRIUM PHASES

The procedure used to determine the empirical functions does not guarantee that the experimentally observed ordered phases will, in fact, be the most stable ones theoretically. Therefore, a portion of the theoretical phase diagram for the Ni–Al alloy system has been determined to test the applicability of these functions. Since our objective is to understand the properties of Ni_3Al, the equilibrium phases have been determined for the range of compositions with less than 50% Al for a temperature of 1000 K. Two approaches will be used to determine the ordered phases of the model system. First, the zero-temperature energetics of various ideal ordered and disordered atomic arrangements are computed to ensure that the experimentally observed structures have the lowest energy of those tested. The second approach is Monte Carlo simulation. Examination of the structures that anneal in during the course of the simulation reveals the equilibrium structures of the model system. Further, as will be described below, the simulations can provide an estimate of the location of the phase boundaries between the single phase regions and coexistence regions of the phase diagram.

The experimental phase diagram[1] for the Ni–Al alloy system is sketched in Fig. 1. There are three phases observed for the Ni-rich half of the phase diagram. The Ni-rich solid solution phase has a fcc crystal structure.

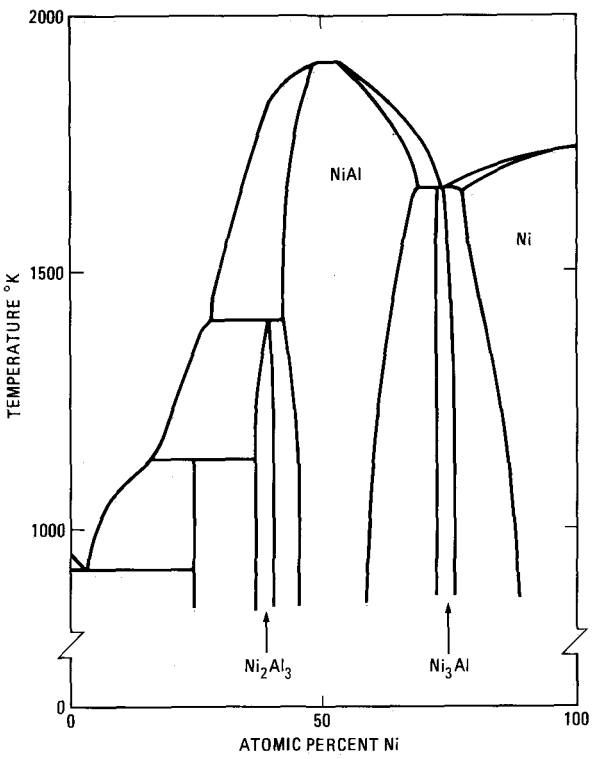

FIG. 1. The experimental phase diagram of the Ni–Al alloy system from Ref. 1.

It is stable for Ni concentrations above about 89% Ni at 1000 K and above about 82% Ni at 1500 K. (All compositions are in atomic percent.) The next phase in increasing Al content is the ordered Ni_3Al phase with the Cu_3Au ($L1_2$) structure. This phase is a fcc structure in which the Ni atoms are located on the cubic faces and the Al atoms are located on the corners of the cubes. The phase diagram shows that this phase is stable up to its melting point of 1660 K and has a range of homogeneity from 72.5%–77% Ni at low temperatures. The third phase is NiAl, which has the ordered CsCl (B2) structure. This is a body-centered cubic (bcc) arrangement of the atoms with one species occupying the center sites and the other occupying the corner sites of the cubic cell. Its range of homogeneity extends up to around 60% Ni at 1000 K with a maximum Ni content of 69.5% at 1670 K. The range of homogeneity decreases at still higher temperatures to the melting point of 1910 K.

The minimum energy of various possible structures based on the fcc, bcc, and hexagonal-close-packed (hcp) lattices was computed at 50% and 75% Ni to ensure that the observed structures did indeed have the lowest energy. In both cases the correct ordered structure had the lowest energy of the simple ordered structures considered. The energy of the ordered structures was also compared with the energy of fcc and bcc lattices where the occupation of the sites by the two species was chosen at random. This corresponds to solid solution phases with no short-range order. For NiAl the ordered structure was 0.15 eV/atom lower in energy than the compositionally random structure, and for Ni_3Al the ordered structure was 0.09 eV lower in energy. Both of these values are consistent with the ordered phases being stable to fairly high temperatures. This result is consistent with the phase diagram, which shows melting of the ordered phases rather than disordering in the solid state.

A more detailed test of the predictions of these potentials concerning the equilibrium phase diagram of the alloy is obtained from the Monte Carlo simulations. The simulations performed here produce the equilibrium atomic structure for a given temperature, pressure, and relative chemical potential of the two species. Recall that for a given temperature and pressure, the composition of an alloy can be considered a function of the chemical potentials of the two species. For alloy compositions in the single phase regions of the phase diagram, the composition varies continuously with the chemical potentials. However, the composition does not change continously with the chemical potentials at positions corresponding to the boundaries of the single phase regions. Since the chemical potentials of two coexisting phases must be the same, the composition of the alloy as a function of the chemical potentials must change discontinuously as the chemical potential of one species is changed from just below to just above the value required for the coexistence of the two phases. Thus a series of simulations performed for different relative chemical potentials, but at the same temperature and pressure, should show a discontinuity in the composition versus chemical potential curve at the chemical potentials of the various phase transitions. The compositions computed on the two sides of the discontinuity correspond to the compositions of the two coexisting phases in the two-phase regions of the phase diagram. Thus the equilibrium phases can be determined by simply observing which structures anneal in during the course of the simulation and the limits of the range of homogeneity of each phase can be determined by noting the compositions at which the structure obtained changes as a function of chemical potential.

There are two practical limitations to this idealized procedure. First, the finite size of the sample in the computer simulation results in the rounding out of the discontinuities. Thus the determination of the compositions on either side of the discontinuity can only be approximate. Second, even though the simulation must ultimately reach the equilibrium structure, if the simulation is started in a metastable state the simulation may not converge to the true equilibrium during the course of any practical computer simulation. Despite these limitations, approximate phase boundaries for the model system can be deduced from the Monte Carlo simulations and compared with the experimental phase diagram.

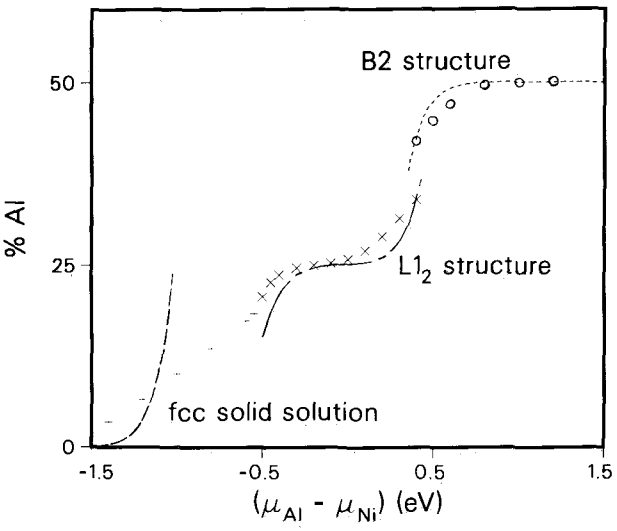

FIG. 2. The equilibrium composition computed by Monte Carlo simulations as a function of the difference in the chemical potentials of Al and Ni for zero pressure and 1000 K. The different symbols designate the structure of the alloy, (+) fcc solid solution, (×) $L1_2$ (Cu_3Au) structure, and (O) B2 (CsCl) structure. The curves represent the compositions predicted by assuming noninteracting substitional impurities antisite defects.

The composition and structure predicted by the Monte Carlo simulations as a function of relative chemical potential at 1000 K and for zero pressure are presented in Fig. 2. (The discrete points represent the compositions obtained from the simulations with the symbol type designating the structure that was obtained in the simulation. The curves represent a simple model for the composition based on defect energies which will be described below.) The simulations were performed for a periodically extended cell with 256 atoms and each simulation considered ten million configurations. For low values of the Al chemical potential, a fcc solid solution phase was obtained in the simulations. For increasing values of the relative chemical potential, $(\mu_{Al} - \mu_{Ni}) \approx -0.5$ eV, there is a small jump in the composition and also a transition from a random distribution of the Al atoms into the ordered $L1_2$ phase. From this the limit of homogeneity of the solid solution phase is estimated to be about 18% Al and the Ni-rich limit of the range of homogeneity of the Ni_3Al phase is estimated to be about 22% Al. It is important to note that the experimentally observed ordered $L1_2$ phase annealed in from compositionally random starting configurations during these simulations. This demonstrates that this model does, in fact, correctly predict the existence of the experimentally observed Ni_3Al structure for compositions near 25% Al.

As the relative chemical potential is increased further, the atoms continue to anneal into lattices with the ordered $L1_2$ structure but with slowly increasing amounts of Al until there is a large jump in the composition and the ordering obtained in the simulations switches to the B2 structure of the NiAl phase for $(\mu_{Al} - \mu_{Ni}) \approx 0.5$ eV. This demonstrates that the model correctly predicts the existence of the ordered B2 phase for composition around 50% Al. This transition between the Ni_3Al structure and the NiAl structure is more difficult to analyze quantitatively because there is a change from a fcc to a bcc structure. Thus the problem of metastability is much greater. It was found though that for increasing Al chemical potential, simulations starting with a fcc lattice of atoms spontaneously distort into the ordered B2 structure. (The simulations allow the three edges of the cell to vary independently, so it is possible for the system to make this transition.) Also, simulations starting with a bcc lattice of atoms distort into the $L1_2$ structure if the relative chemical potential is lowered. There is a small range of relative chemical potentials, though, where the simulations will stay in either the B2 or $L1_2$ structure depending on the starting point of the simulation. The phase transition should occur somewhere in this range. Thus the boundaries of the two-phase region at 1000 K should be located at compositions of about 34% Al and about 42% Al, which is in reasonable agreement with experiment.

The behavior of the composition as a function of chemical potential for the two ordered phases can be compared with that predicted by the energetics of creating substitutional impurities in the solid solution case or antisite defects, i.e., Ni atoms in Al sites or Al atoms in Ni sites, in the ordered structures. The solid curves in Fig. 2 were obtained by assuming that these defects are noninteracting. Namely, that the energy to create an antisite defect or substitutional impurity is not affected by the presence of other defects and that the entropy associated with the defects is ideal. The energies of the defects are computed at 0 K. This simple picture provides a good description of the variation of the composition with chemical potential for the two ordered phases NiAl and Ni_3Al indicating that the antisite defects are nearly independent in these cases. For the solid solution phase, the comparison between this simple model and the simulations is poor, indicating that there is a strong interaction between the impurities in the solid solution alloy.

The above calculations show that the theoretical model predicts the existence of a Ni-rich fcc solid solution phase, an ordered $L1_2$ phase for compositions around 75% Ni and an ordered B2 phase for compositions around 50% Ni. This is in agreement with the experimental data. Further, the Monte Carlo simulations provide an estimate of the range of homogeneity of these phases at 1000 K, which can then be compared with the experimental phase diagram (Fig. 1). The NiAl phase extends up to about 58% Ni. The Ni_3Al phase extends from about 66% Ni to about 78% Ni. Finally, the Ni-rich solid solution phase extends from 82% Ni up to pure Ni. The range of homogeneity predicted for the Ni-rich solid solution phase is somewhat wider than found experimentally, but the overall agreement with experiment is quite reasonable. The good agreement between the experimentally observed phases and the theoretical predictions based on the EAM energies provides strong evidence for the reliability of the embedding functions and core–core repulsions used in this work.

IV. ELASTIC CONSTANTS AND VIBRATIONAL PROPERTIES

The elastic properties of the alloy are important to the mechanical behavior of the material. Therefore the comparison of the elastic constants computed from this model with the experimental values is a crucial test of the empirical functions used here and a good indicator of their predictive value. In addition, the phonon dispersion curves of the material reflect more details of the atomic interactions than are contained in the elastic constants. We have therefore calculated the elastic constants of Ni_3Al as well as the phonon dispersion curves and vibrational density of states. The calculated elastic

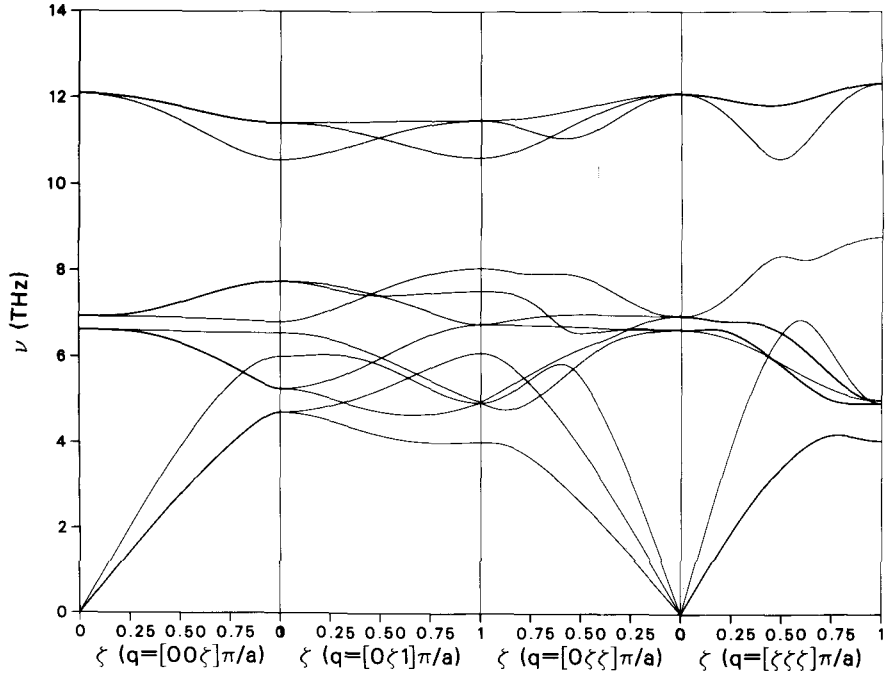

FIG. 3. The calculated phonon dispersion curves for Ni_3Al. The wave vector is mapped out along four high-symmetry directions in the cubic crystal.

constants for Ni_3Al are then compared with the measured values.

The phonon modes of Ni_3Al have been calculated by computing the dynamical matrix from Eq. (1) as was done for pure metals by Daw and Hatcher.[9] The extension of this procedure to heteronuclear systems is straightforward, albeit algebraically tedious. The resulting phonons modes are plotted in Fig. 3 along high symmetry directions in the cubic Brillouin zone. The low-energy modes (i.e., the acoustical modes) involve approximately equal amplitudes for Ni and Al atoms, as is to be expected. The modes around 6–8 THz are optical modes involving mostly Ni and very little Al motion. The highest energy modes (near 12 THz) are optical modes involving mostly Al and very little Ni motion. An interesting feature of the phonons is the apparent gap in the modes around 8–10 THz.

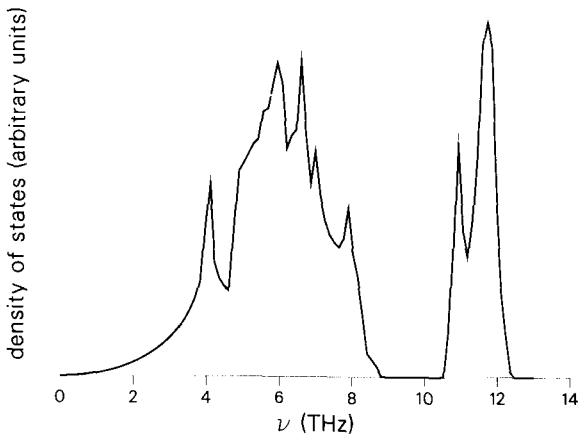

FIG. 4. The calculated vibrational density of states computed for Ni_3Al.

The gap in vibrational modes is made more apparent in Fig. 4, where we have calculated the density of vibration states for Ni_3Al. The density of states was computed using 73 150 points in the irreducible part of the Brillouin zone and is converged with the number of integration points. The structure observed in the density of states is, therefore, real. Unfortunately, the authors are unaware of any measurements of either the phonon dispersion relations or the phonon density of states for Ni_3Al. The measurement of these properties would provide valuable information for testing this or other atomic models of Ni_3Al.

From the long-wavelength limit of the acoustical modes in Fig. 3, the elastic constants can be computed. The longitudinal and transverse modes along the [100] direction and one of the transverse modes along the [110] direction are sufficient to determine C_{11}, C_{12} and C_{44}, and the other modes along [110] and [111] are used as checks. The calculated elastic constants are

TABLE IV. Calculated elastic constants of Ni_3Al and experimental values. The elastic constants are in 10^{12} ergs/cm^3.

	Theory (EAM)	Experiment (Ref. 23)
C_{11}	2.516	2.302
C_{12}	1.370	1.493
C_{44}	1.262	1.316

compared to experiment in Table IV. The agreement is quite good and again gives confidence in the reliability of the empirical functions.

V. POINT DEFECTS

The properties of point defects, particularly vacancies and antisite defects, are of interest because they are closely related to diffusion in the bulk material. Care must be taken, though, in determining the appropriate formation energies for defects in ordered alloys. For pure metals the atom removed to form a vacancy can simply be added to the metal somewhere else in the system. The problem in the ordered alloys is that if several vacancies are created on the same sublattice, then antisite defects must be created, or existing antisite defects destroyed, when those atoms are used to create more bulk metal. Thus the formation energy of vacancies includes a contribution from the energy required to create antisite defects.

The thermal concentration of defects can most easily be derived by working in an ensemble with fixed temperature and chemical potentials μ_i. The concentrations of the defects will be assumed to be small so that the defects can be treated as noninteracting. Consider a system with N lattice sites that are divided into two sublattices designated by A and B for the element that normally resides on that sublattice. In particular, for an A_3B alloy, there are three A sites for each B site. Each lattice site will be occupied either by an atom appropriate to the sublattice, by a vacancy, or by an atom of the opposite type. For noninteracting defects, the energy of the system is

$$\frac{E}{N} = \frac{E_0}{N} + n_A^v E_A^v + n_B^v E_B^v + n_{AB} E_{AB} + n_{BA} E_{BA}, \quad (10)$$

where E_0 is the energy of the ideal lattice, n_A^v is the number of vacancies on the A sublattice divided by the total number of lattice sites, E_A^v is the difference in energy between the ideal lattice and the lattice with a vacancy on the A sublattice, n_{AB} is the number of A sublattice sites occupied by a B atom (antisite defect) divided by the total number of lattice sites, E_{AB} is the energy difference between the lattice with a single B atom substituted for an A atom and the ideal lattice, and the other terms have analogous meanings. The values of these defect energies are given in Table V. The configurational entropy of the system is given by

$$\frac{S}{N} = \frac{3}{4}\left[s\left(\frac{4}{3} n_{AB}\right) + s\left(\frac{4}{3} n_A^v\right)\right] + \tfrac{1}{4}\left[s(4n_{BA}) + s(4n_B^v)\right], \quad (11)$$

where s is the ideal entropy function

$$s(x) = -[x \ln(x) + (1-x)\ln(1-x)]. \quad (12)$$

TABLE V. Defect energy ΔE, formation volume V^f, and migration energy E^m of vacancies and antisite defects in Ni_3Al. The defect energy is the energy difference between the lattice with the defect and the ideal crystal with the same number of lattice sites. Its relationship to vacancy formation energies is discussed in the text. Here Ω is the volume per atom of the ideal lattice. The value in parentheses is an experimental result from Ref. 24.

	ΔE (eV)	V^f/Ω	E^m (eV)
Ni vacancy	6.10	0.95	1.02 (to Ni site) (1.2 ± 0.2)
			1.28 (to Al site)
Al vacancy	6.55	0.82	0.91 (to Ni site)
Ni→Al antisite defect	0.58	0.33	
Al→Ni antisite defect	0.54	−0.21	

(Here and in the following, temperatures will be assumed to be in units such that the Boltzman constant k_B equals 1.) With these definitions the total number of A atoms, N_A, is then given by

$$N_A = N(\tfrac{3}{4} - n_A^v + n_{BA} - n_{AB}) \quad (13)$$

and similarly for N_B with the factor of $\frac{3}{4}$ changed to $\frac{1}{4}$. Minimization of the grand potential $E - TS - \Sigma \mu_i N_i$, with respect to the different defect concentrations, then yields for the antisite concentration

$$n_{AB} = \frac{3}{4}\left(\frac{e^{-(E_{AB}+\mu_A-\mu_B)/T}}{1+e^{-(E_{AB}+\mu_A-\mu_B)/T}}\right) \quad (14)$$

and gives for the vacancy concentration

$$n_A^v = \frac{3}{4}\left(\frac{e^{-(E_A^v+\mu_A)/T}}{1+e^{-(E_A^v+\mu_A)/T}}\right), \quad (15)$$

with similar expressions for the defects on the B lattice

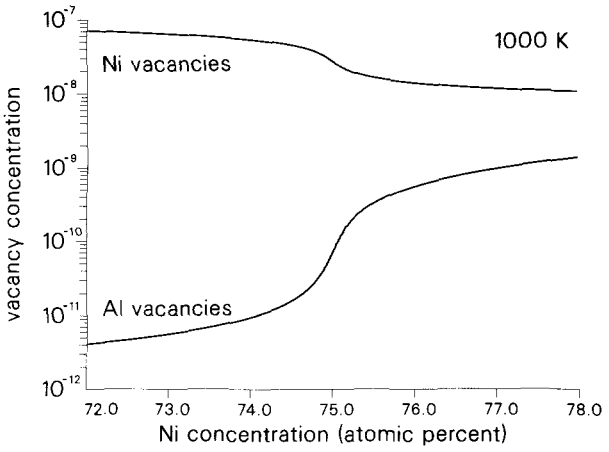

FIG. 5. The calculated concentration of Ni and Al vacancies at 1000 K as a function of bulk composition based on the defect energies in Table V.

with the $\frac{3}{4}$ replaced by $\frac{1}{4}$. Finally, one of the chemical potentials can be eliminated by noting the relationship between the Gibb's free energy and the chemical potentials, which gives, for zero pressure,

$$\mu_A N_A + \mu_B N_B = E - TS, \quad (16)$$

where the energy is given by Eq. (10) and the entropy by Eq. (11).

With these results it is possible to determine the vacancy concentration for a given alloy composition and temperature by adjusting one of the chemical potentials to obtain the desired bulk composition and then computing the vacancy concentration on each sublattice from Eq. 15. The result of this procedure for a temperature of 1000 K using the defect energies quoted in Table V is shown in Fig. 5. Note that the concentration of vacancies is much larger on the Ni sublattice than on the Al sublattice. This is in agreement with the positron annihilation study by Dasgupta *et al.*,[25] which suggested that well-annealed samples of Ni_3Al contain some Ni vacancies but do not contain Al vacancies. Second, the vacancy concentration changes significantly near the ideal composition with more vacancies found for Al-rich alloys.

The vacancy formation energy for Ni_3Al has been determined by positron annihilation studies by Wang *et al.*[24] They fit the vacancy concentration to an exponential form and deduced an activation energy of 1.6 ± 0.2 eV for the formation of thermal vacancies. This value should be compared to the value of $E^v_A + \mu_A$ appropriate to the alloy at ideal Ni_3Al composition (see Eq. 15). Ideal composition corresponds to setting $n_{AB} = n_{BA}$, which implies that $\mu_A - \mu_B = (E_{BA} - E_{AB})/2$ in the limit of zero temperature. Combining this result with Eq. (16) in the zero-temperature limit yields $\mu_A = E_0(E_{BA} - E_{AB})/8$. Thus the vacancy formation energy predicted for thermal Ni vacancies is 1.47 eV in good agreement with the experimental results. It is important to note that for ordered alloys, the vacancy formation energy, in general, depends on the overall composition as can be seen from the variation of the vacancy concentration with composition that is shown in Fig. 5.

The formation volumes of the various defects have been computed and are shown in Table V. This is the difference between the volume of a lattice containing N atoms and the defect and N times the average volume per atom of the ideal lattice. The binding energies of divacancies has also been computed. The Ni–Ni vacancy pairs are bound by 0.16 eV relative to the separated vacancies while Ni–Al vacancy pairs are bound by 0.18 eV. The computed vacancy migration energies are also listed in Table V. Note that for ordered alloys there are different vacancy migration energies depending on whether or not the vacancy moves to a site on the same sublattice. The migration energy of a Ni vacancy into an adjacent Ni site is in agreement with the value obtained by Wang *et al.*[24] The two antisite defects are found to have very similar energies. This is again in agreement with the work of Dasgupta *et al.*[25] where they deduced the presence of both kinds of defects in their annealed crystals.

VI. ANTIPHASE BOUNDARIES

One of the interesting features of nickel aluminide is its increase in yield stress with increasing temperature. Pope and Ezz[26] have recently argued that the cross-slip model due to Kear and Wilsdorf[27] and refined by Takeuchi and Kuramoto[28] is the most successful explanation of this anomalous temperature dependence. This model requires that there is a strong anistropy between the energy of the (100) and (111) antiphase boundary energies. These energies have been calculated by minimizing the energy of a rectangular cell with periodic boundary conditions that contained two parallel antiphase boundaries. The length of the cell (about 35 Å) was varied to ensure that there was no significant interaction between the two boundaries in the cell. The calculated energy for the (100) boundary is 28 ergs/cm^2 and that for the (111) boundary is 96 ergs/cm^2. The preference for (100) boundaries is in agreement both with the requirements of the cross-slip model as well as with the recent rapid solidification studies by Horton and Liu.[29]

The lower energy for the (100) boundary is not surprising if one considers the changes in local environment at the boundary. For the (100) boundary, the nearest-neighbor environment of the boundary atoms is the same as for the bulk, and the differences only occur at second and greater neighbor distances. For the (111) boundary, the nearest-neighbor environment of the boundary atoms is changed. Because the majority of the energy of the solid is associated with the nearest-neighbor interactions, the (100) boundary would be expected to be favored.

VII. SURFACES

There has been recent interest in the surfaces of Ni–Al alloys. Due to the crystal structure of these alloys, some of the low index faces have two possible bulk terminated surfaces. The determination of the preferred termination is thus of interest, in addition to the usual interest in the atomic relaxation at the surface. Davis and Noonan[30] have used low-energy-electrondiffraction (LEED) to study the (110) face of NiAl and found a rippling of the atoms in the top layer. Sondericker *et al.*[31,32] have used both LEED and theoretical calculations to show that the preferred (100) surface of Ni_3Al is terminated on the mixed composition plane and that there is again a slight rippling of the top atomic plane.

In this work the surface energy and atomic relaxations are calculated for the various possible bulk terminations of the three low index surfaces of Ni_3Al. (There has been no effort in this work to search for possible reconstruction of these surfaces.) For the (100) surface there are two possible termination planes, one with all Ni atoms and the other with equal number of Ni and Al atoms. The surface energy for termination on the mixed composition plane is 1620 ergs/cm^2, while for termination on the pure Ni plane the surface energy is 1885 ergs/cm^2. The lower energy of the mixed composition surface is in agreement with the results of Sondericker *et al.*[31,32] The surface relaxations calculated for the mixed composition surface are small. All the atoms are close to their bulk sites except for the Al atoms in the top layer, which are relaxed outward by 0.06 Å. The prediction of a small rippling of the surface is in agreement with the LEED results of Sondericker *et al.*[31,32] They find that the second layer atoms are at bulk positions, the top layer Ni atoms are relaxed inward by 0.05 $\pm$ 0.03 Å, and the Al atoms sit 0.02 $\pm$ 0.03 Å above the Ni atoms.

The (110) face of Ni_3Al also has two possible terminations, one with only Ni atoms and the other with an equal mix of the two species. The surface energy for termination on the pure Ni plane is 1920 ergs/cm^2 and for the mixed composition plane is 1730. Thus termination on the mixed composition plane is preferred. All of the relaxed atomic positions are with 0.005 Å of their bulk values, except for the top layer Al atoms that are relaxed outward 0.06 Å and the third layer Al atoms that are relaxed inward by 0.01 Å.

There is only one bulk termination for the (111) surface of Ni_3Al. The surface energy calculated for this face is 1645 ergs/cm^2. The relaxed atomic positions are again all with 0.005 Å of bulk values with the exception of the top layer Al atoms that are relaxed out 0.06 Å and the second layer Al atoms that are relaxed inward 0.01 Å.

VIII. SUMMARY

The empirical determination of the embedding functions and core–core repulsions for Ni and Al used by the EAM has been presented. The reliability of this parametrization has then been tested by computing the equilibrium phases of the Ni–Al system at 1000 K. The good agreement between the theoretically predicted phases and the experimentally observed phases provides good evidence that this method provides a reasonable description of the Ni–Al alloy. Another verification of the reliability of the method has been found in the good agreement between the computed and experimental elastic constants for Ni_3Al. We have also computed the phonon dispersion curves and vibrational density of states of Ni_3Al and have found a gap in the density of states around 9–10 THz. The point defect properties of Ni_3Al have been computed in agreement with experiment. The formation energy of vacancies on the Ni lattice is found to be smaller than that for Al vacancies and the energy of the two types of antisite defects are found to be comparable. The energy of the (100) antiphase boundary is found to be less than the energy of the (111) antiphase boundary in accord with the requirements of the cross-slip model for the anomalous temperature dependence of the yield stress. Finally, the surface energy associated with different possible bulk terminations of the low index faces of Ni_3Al have been computed. For the (100) and (110) faces, the mixed composition plane is energetically preferred. Future work with this method will concentrate on the detailed structure, including compositional variations, of grain boundaries in Ni_3Al.

ACKNOWLEDGMENT

This work was supported by the U.S. Department of Energy, Office of Basic Energy Sciences.

REFERENCES

[1]M. Hansen, *Constitution of Binary Alloys* (McGraw-Hill, New York, 1958).
[2]P. H. Thorton, R. G. Davis, and T. L. Johnson, Metall. Trans. **1**, 207 (1970).
[3]E. A. Aitken, *Intermetallic Compounds*, edited by J. H. Westbrook (Wiley, New York, 1967), pp. 491–515.
[4]C. T. Liu, C. L. White, and J. A. Horton, Acta Metall. **33**, 213 (1985).
[5]M. S. Daw and M. I. Baskes, Phys. Rev. B **29**, 6443 (1984).
[6]M. S. Daw, Surf. Sci. Lett. **166**, L161 (1986).
[7]S. M. Foiles, M. I. Baskes, and M. S. Daw, Phys. Rev. B **33**, 7983 (1986).
[8]M. S. Daw, M. I. Baskes, C. L. Bisson, and W. G. Wolfer, in the proceedings of The Special Symposium on Modelling Environmental Effects on Crack Initiation and Propagation, TMS-AIME, Toronto, Canada, October 1984.
[9]M. S. Daw and R. L. Hatcher, Solid State Comm. **56**, 697 (1985).
[10]S. M. Foiles, Phys. Rev. B **32**, 3409 (1985).
[11]S. M. Foiles, Phys. Rev. B **32**, 7685 (1985).
[12]T. E. Felter, S. M. Foiles, M. S. Daw, and R. H. Stulen, Surf. Sci. Lett. **171**, L379 (1986).
[13]R. A. Johnson, Phys. Rev. B **6**, 2094 (1972).
[14]M. S. Daw (in preparation).
[15]J. H. Rose, J. R. Smith, F. Guinea, and J. Ferrante, Phys. Rev. B **29**, 2963 (1984).
[16]E. Clementi and C. Roetti, At. Data Nucl. Data Tables **14**, 177 (1974).
[17]K. Fuchs, Proc. R. Soc. London, Ser. A **153**, 622 (1936); **157**, 444 (1936).
[18]A. Englert, H. Tompa, and R. Bullough, *Fundamental Aspects of Dislocation Theory* (National Bureau of Standards, Washington, DC, 1970).
[19]W. Wycisk and M. Feller-Kneipmeier, J. Nucl. Mater. **69&70**, 616 (1978).
[20]R. W. Balluffi, J. Nucl. Mater. **69&70**, 240 (1978).
[21]R. Hultgren, P. D. Desai, D. T. Hawkins, M. Gleiser, and K. K. Kelly, *Selected Values of the Thermodynamic Properties of Binary Alloys* (American Society for Metals, Metals Park, OH, 1973).
[22]W. W. Wood, J. Chem. Phys. **52**, 729 (1970).

[23]M. H. Yoo (private communication). The experimental values at $T = 0$ K are obtained by scaling the room temperature values reported by F. X. Kayser and C. Stassis, Phys. Status Solidi A **64**, 335 (1981). The scaling was accomplished by comparison to the temperature dependence of the elastic constants as measured by K. Ono and R. Stern, Trans. AIME **245**, 171 (1969).
[24]T. Wang, M. Shimotomai, and M. Doyama, J. Phys. F **14**, 37 (1984).
[25]A. Dasgupta, L. C. Smedskjaer, D. G. Legnini, and R. W. Siegel, Mater. Lett. **3**, 457 (1985).
[26]D. P. Pope and S. S. Ezz, Int. Metall. Rev. **29**, 3 (1984).
[27]B. H. Kear and H. G. F. Wilsdorf, Trans. TMS-AIME **224**, 382 (1962).
[28]S. Takeuchi and E. Kuramoto, Acta Metall. **21**, 415 (1973).
[29]J. A. Horton and C. T. Liu, Acta Metall. **33**, 2191 (1985).
[30]H. L. Davis and J. R. Noonan, Phys. Rev. Lett. **54**, 566 (1985).
[31]D. Sondericker, F. Jona, V. L. Moruzzi, and P. M. Marcus, Solid State Comm. **53**, 175 (1985).
[32]D. Sondericker, F. Jona, and P. M. Marcus, Phys. Rev. B **33**, 900 (1986).